Three-dimensional optical correlator with general complex filters

Youzhi Li and Joseph Rosen

A new type of electro-optical three-dimensional (3-D) correlator is proposed and demonstrated. A 3-D object scene, observed by multiple cameras from several points of view, is correlated with a 3-D complex computer-generated function. This correlator is a hybridization of the joint transform and the VanderLugt correlators, and, as such, it allows correlations to be made between 3-D real-world objects and 3-D general complex functions. Experimental results are presented. © 2000 Optical Society of America

OCIS codes: 070.4450, 070.2580, 070.5010, 070.6110, 100.5090.

1. Introduction

Three-dimensional (3-D) spatial correlations can be made fast and in parallel by the use of optics. In 1997 Rosen extended the optical correlator's operation from two dimensions to three.[1] This correlation involves fusing images of objects from a few different points of view and allows objects to be identified and located in 3-D space. This process has been demonstrated in a 3-D joint transform correlator (JTC), in which a reference and tested objects are observed together from a distance.[2,3] The reference object and the tested objects are projected a few times from different points of view onto a spatial light modulator (SLM), and the projected images are electro-optically processed to yield the desired 3-D correlation. Recently two other attempts at 3-D optical pattern recognition were reported.[4,5] Although these creative proposals contribute original ideas to the reservoir of image-processing techniques, none of them has permitted complete spatial correlation in all three dimensions. Therefore they have the property of shift invariance only in the transverse plane and not along the longitudinal axis. When the observed object is shifted along the longitudinal axis from the position for which its filter has been designed, the correlation peak either disappears[4] or remains at the same location.[5] Therefore these systems are not capable of locating specific objects in a 3-D scene. In our 3-D correlator, however, when the observed object is shifted along the longitudinal axis the correlation peak is proportionally shifted along the same axis and thus permits the object to be located in all the coordinates of the 3-D space. We have proposed a distortion-invariant version of the 3-D correlator.[6] Algorithms of distortion-invariant pattern recognition usually require the use of correlators with complex or real bipolar reference functions. A new design for 3-D correlators that operate with any complex reference functions is the topic of this study.

Like most two-dimensional (2-D) JTC's, the 3-D JTC is limited by the use of positive real-valued reference functions. That is so because most spatial light modulators (SLM's), used today as input transparency masks in JTC's, cannot simultaneously provide amplitude and phase modulation with satisfactory quality. However, many schemes for pattern recognition and other image-processing tasks require complex or at least bipolar real reference functions. A possible solution to this problem can be holographic coding at the JTC input plane. In that case, the tested object is sampled by a grating and appears side by side with a computer-generated hologram used as the reference function.[7,8] These systems, however, suffer from low bandwidth, because only at most one third of the available bandwidth actually participates in the process. This drawback causes the loss of the high-resolution information from the observed scene.

Of course, the JTC is not the only available optical correlator. The VanderLught correlator[9] (VLC) was

The authors are with the Department of Electrical and Computer Engineering, Ben-Gurion University of the Negev, P.O. Box 635, Beer-Sheva 84105, Israel. J. Rosen's e-mail address is rosen@ee.bgu.ac.il.

Received 27 March 2000; revised manuscript received 14 August 2000.

0003-6935/00/356561-12$15.00/0

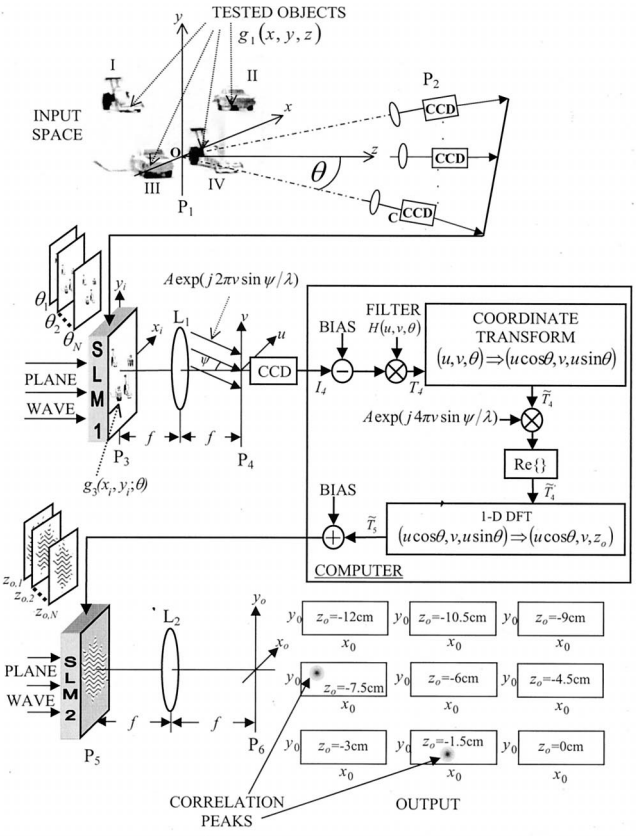

Fig. 1. Schematic of the hybrid 3-D correlator. DFT, discrete Fourier transform.

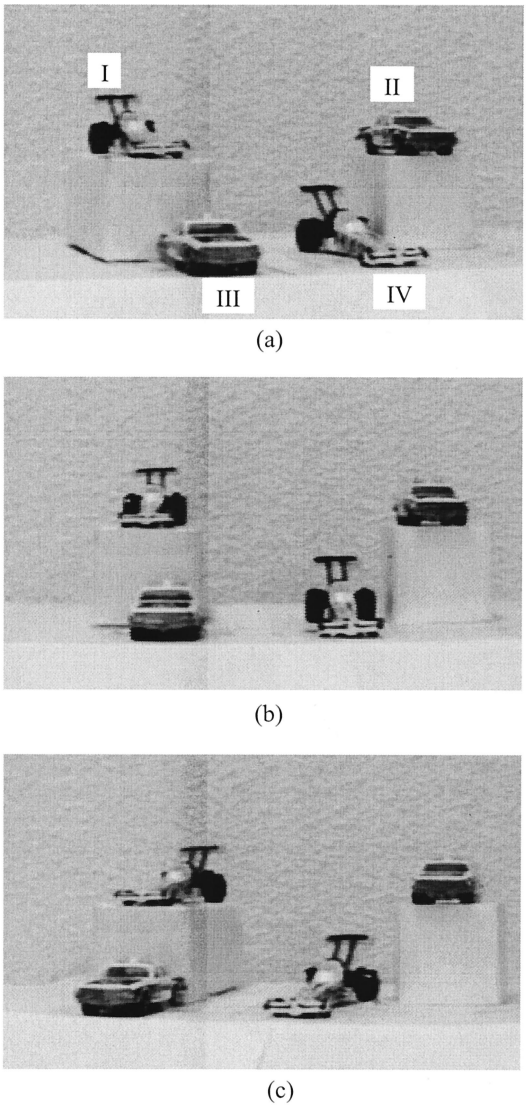

Fig. 2. Three images of thirty-one of the scene as observed from different points of view from plane P_2 at angles (a) $\theta = -15°$, (b) $\theta = 0°$, and (c) $\theta = 15°$.

invented before the JTC and is still in common use today.[10] A VLC equipped with a Fourier hologram can correlate the input image with a general complex reference function. However, the main drawback of the VLC for our purposes is its inability to process the image's spatial spectrum digitally. When one tries to record the spectrum distribution into a digital processor with any camera, the phase function, which usually contains the object's shape information, is lost. As is shown in what follows, digital processing is a crucial part of our 3-D correlation scheme. Therefore a new correlator design is required in which the benefits of both classic correlators, the VLC and the JTC, are combined. Such a correlator is described here.

We propose a technique that is similar, but not identical, to one that was employed previously for 2-D correlators[11] in which a camera records electronic Fourier holograms of the input scene and transfers them into a computer. Thus, although the hologram distributions are real and positive valued, the complete complex information of the spatial spectrum is recorded into the computer and can be digitally processed. In addition to being digital processed, the spectrum is multiplied by a filter function in the Fourier plane, and an additional Fourier transform (FT) of this product yields the desired correlation results. Such a correlator is actually a combination of a JTC (with a point as the reference function) and a VLC (with a spatial filter at the Fourier plane). As a hybrid configuration it combines the best features of the two types of correlator. Explicitly, it permits an effective complex reference function to be implemented, as is usually possible in a VLC. It also lets us perform complicated digital manipulations (in our case, it is a coordinate transformation, as explained below) of the spatial spectrum of the input function, as is inherently possible with the JTC. To our best knowledge this is the first time that such hybridization has been suggested in the field of 3-D image processing.

2. System Description and Analysis

The 3-D optical correlator is shown in Fig. 1. A 3-D input function $g_1(x, y, z)$ that describes all tested objects in the observed scene is located in coordinate system (x, y, z), where P_1 is the transverse plane $z = 0$. The cameras (or a single camera that moves from

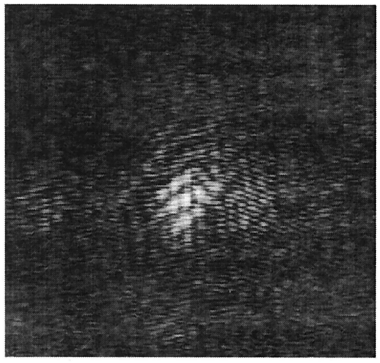

(a)

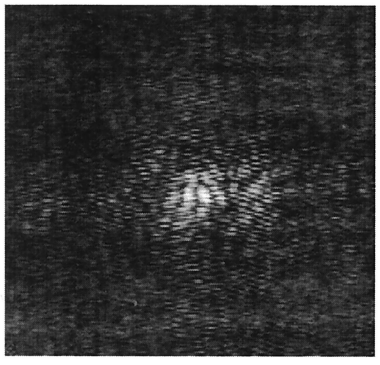

(b)

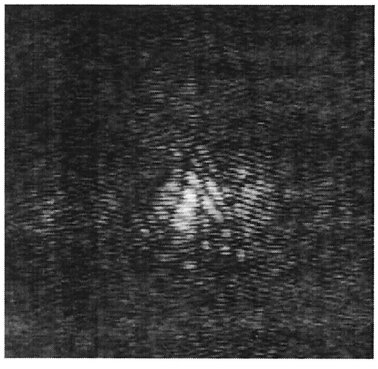

(c)

Fig. 3. Three electronic Fourier holograms of the three images in Fig. 2, as recorded by the CCD at plane P_4.

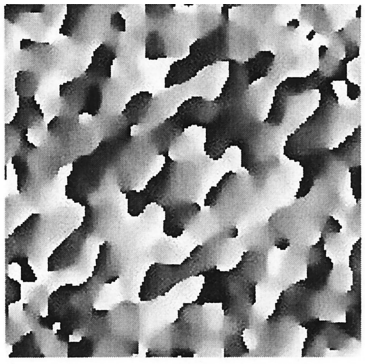

(a)

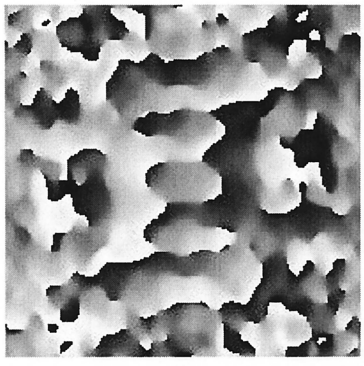

(b)

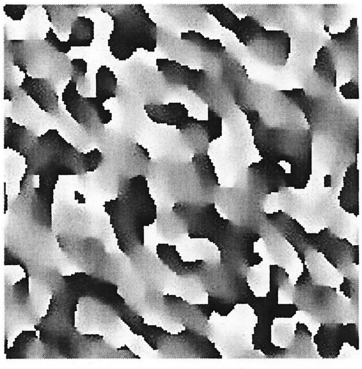

(c)

Fig. 4. Three examples of thirty-one of POF's computed from a single race car observed by the CCD at plane P_2 from angles (a) $\theta = -15°$, (b) $\theta = 0°$, and (c) $\theta = 15°$.

point to point) record the input scene from different points of view along an arc on the x–z plane, whose center is located at the origin point $(x, y, z) = (0, 0, 0)$. From each point of view, the camera observes plane P_1 through an imaging lens located far from plane P_1. In each point of view the line OC between the center of the camera's plane and the origin point $(x, y, z) = (0, 0, 0)$ at the x–z plane is orthogonal to the camera's plane. The angle between the z axis and line OC is denoted θ. For each θ, the projected function $g_3(x_i, y_i; \theta)$ is displayed on SLM1, where (x_i, y_i) are the coordinates of plane P_3. From the geometry of the scene, the relation between (x_i, y_i, θ) and (x, y, z) is given by[3]

$$(x_i, y_i) = M(x \cos \theta + z \sin \theta, y), \tag{1}$$

where M is the magnification factor of the imaging lens. It is assumed that the distance between plane P_1 and the imaging lens is much longer than the depth of the object function $g_1(x, y, z)$, and therefore

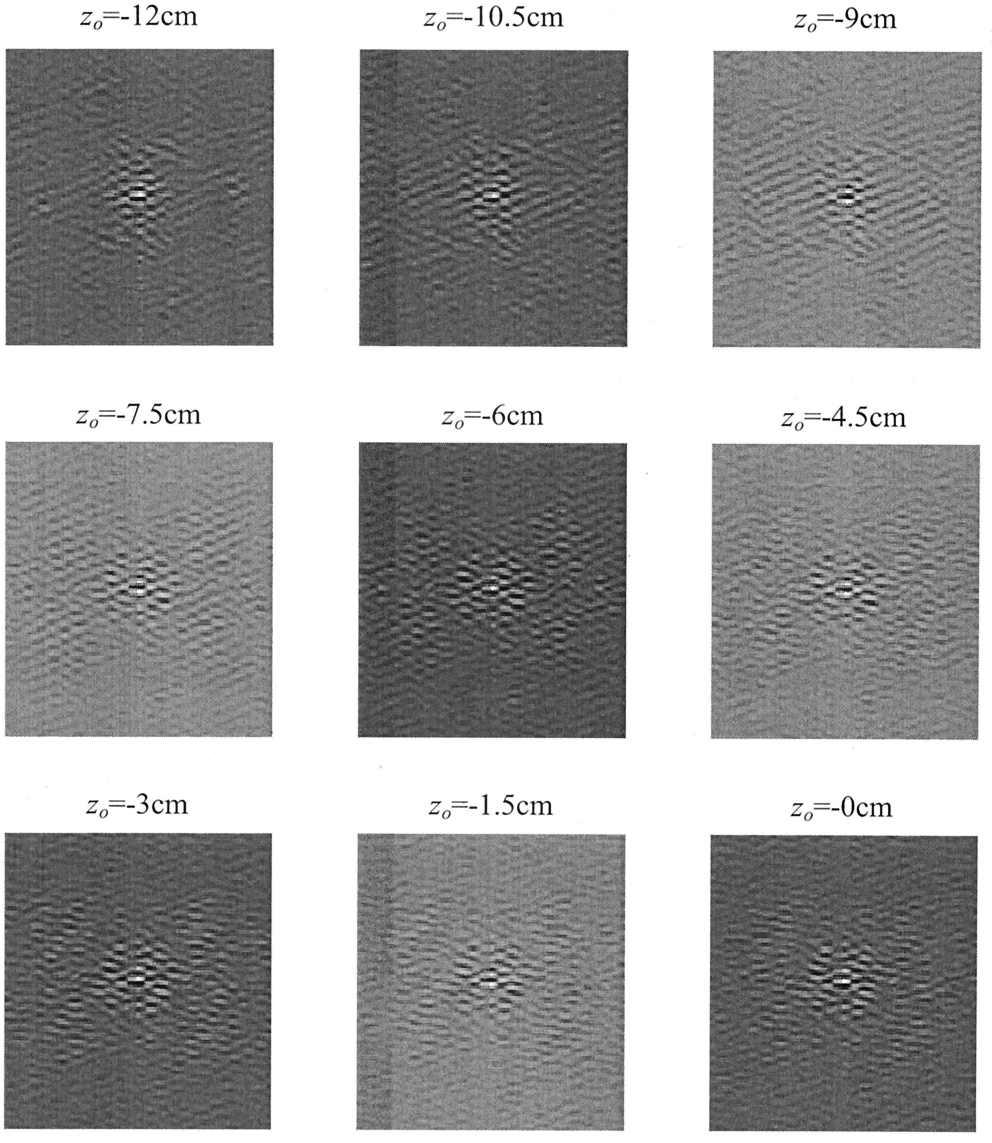

Fig. 5. Nine of sixty-seven holograms displayed on SLM2 for several values of longitudinal axis z_0.

the magnification factor is approximately the same constant M for all the object points.

Next we consider the intensity distribution on plane P_4 for any angle θ. The complex amplitude coming from SLM1 through lens L_1 interferes with a reference plane wave, hitting the CCD plane at an angle ψ from the optical axis on plane v–z. With the 2-D FT relation between planes P_3 and P_4, the intensity on plane P_4 is

$$I_4(u, v, \theta) = \left| A \exp\left(i \frac{2\pi}{\lambda} v \sin \psi \right) + \int_{-\infty}^{\infty} \int_{-\infty}^{\infty} g_3(x_i, y_i; \theta) \times \exp\left[i \frac{2\pi}{\lambda f} (u x_i + v y_i) \right] dx_i dy_i \right|^2, \quad (2)$$

where λ is the optical wavelength, A is a constant, and f is the focal distance of Fourier lens L_1. Let us look now at the intensity distribution $I_4(u, v, \theta)$ as a function of the input object $g_1(x, y, z)$. For a single element, from the entire 3-D object function of size $(\Delta x, \Delta y, \Delta z)$ and brightness $g_1(x, y, z)$, the complex amplitude on plane P_4 is

$$u_4(u, v, \theta) = A \exp\left(i \frac{2\pi}{\lambda} v \sin \psi \right) + g_1(x, y, z) \times \exp\left\{ i \frac{2\pi}{\lambda f} [u x_i(x, z, \theta) + v y_i(y)] \right\} \Delta x \Delta y \Delta z. \quad (3)$$

Equation (3) is the degenerate version of Eq. (2) when there is only a single infinitesimal source point in the scene. Note that $g_1(x, y, z)$ is not a function in this case but a constant, which expresses the brightness of the source point. This single source point in the observed scene induces a point on plane P_3, but for each angle θ the location of this point on plane P_3 is different according to

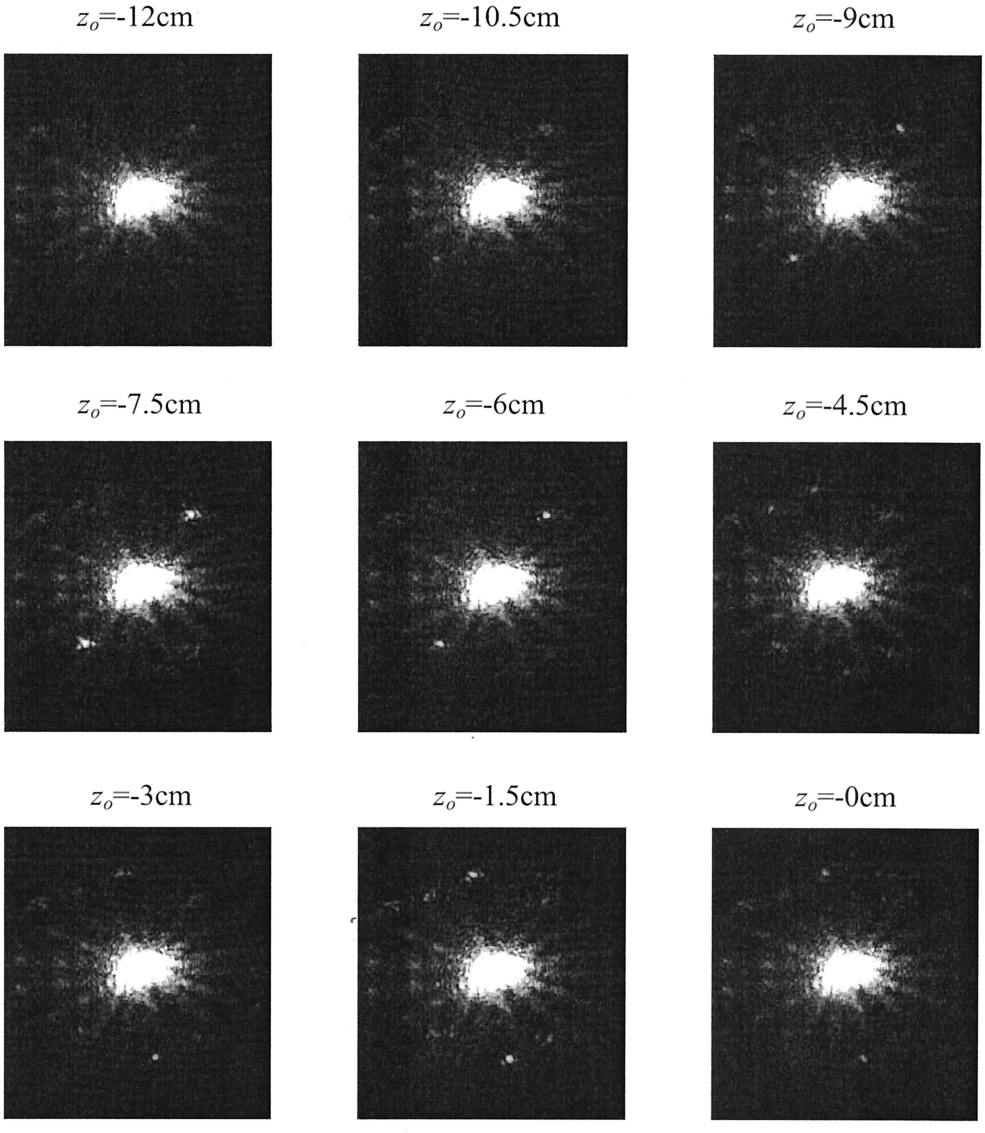

Fig. 6. Nine of the output correlation planes obtained by optical FT of the nine holograms shown in Fig. 5.

Eq. (1). Therefore x_i is actually a function of x, z, and θ, whereas y_i is a function of y, both according to Eq. (1). Substituting Eq. (1) into Eq. (3) yields

$$u_4(u, v, \theta) = A \exp\left(i \frac{2\pi}{\lambda} v \sin \psi\right) + g_1(x, y, z) \times \exp\left[i \frac{2\pi M}{\lambda f} (ux \cos \theta + vy + uz \sin \theta)\right] \Delta x \Delta y \Delta z. \quad (4)$$

Next we examine the influence of all points of the object $g_1(x, y, z)$. Because SLM1 is illuminated by a coherent plane wave, the electromagnetic fields that originate from the input image points are summed. The overall complex amplitude at plane P_4 is

$$u_4(u, v, \theta) = A \exp\left(i \frac{2\pi}{\lambda} v \sin \psi\right) + G_1(u, v; \theta). \quad (5)$$

Because the input object is 3-D, G_1 is obtained by a 3-D integral over all the plane waves from all the object points as follows:

$$G_1(u, v; \theta) = \int_{-\infty}^{\infty} \int_{-\infty}^{\infty} \int_{-\infty}^{\infty} g_1(x, y, z) \exp\left[i \frac{2\pi M}{\lambda f} (ux \cos \theta + vy + uz \sin \theta)\right] dx dy dz. \quad (6)$$

The overall intensity at plane P_4 is

$$I_4(u, v, \theta) = \left|A \exp\left(i \frac{2\pi}{\lambda} v \sin \psi\right) + G_1(u, v; \theta)\right|^2 \quad (7)$$

Apparently $I_4(u, v, \theta)$ contains four terms, but only the third term contains the useful spectrum of $g_1(x, y, z)$. We wish to get rid of all unnecessary terms, but at this stage we can easily get rid of the bias term by

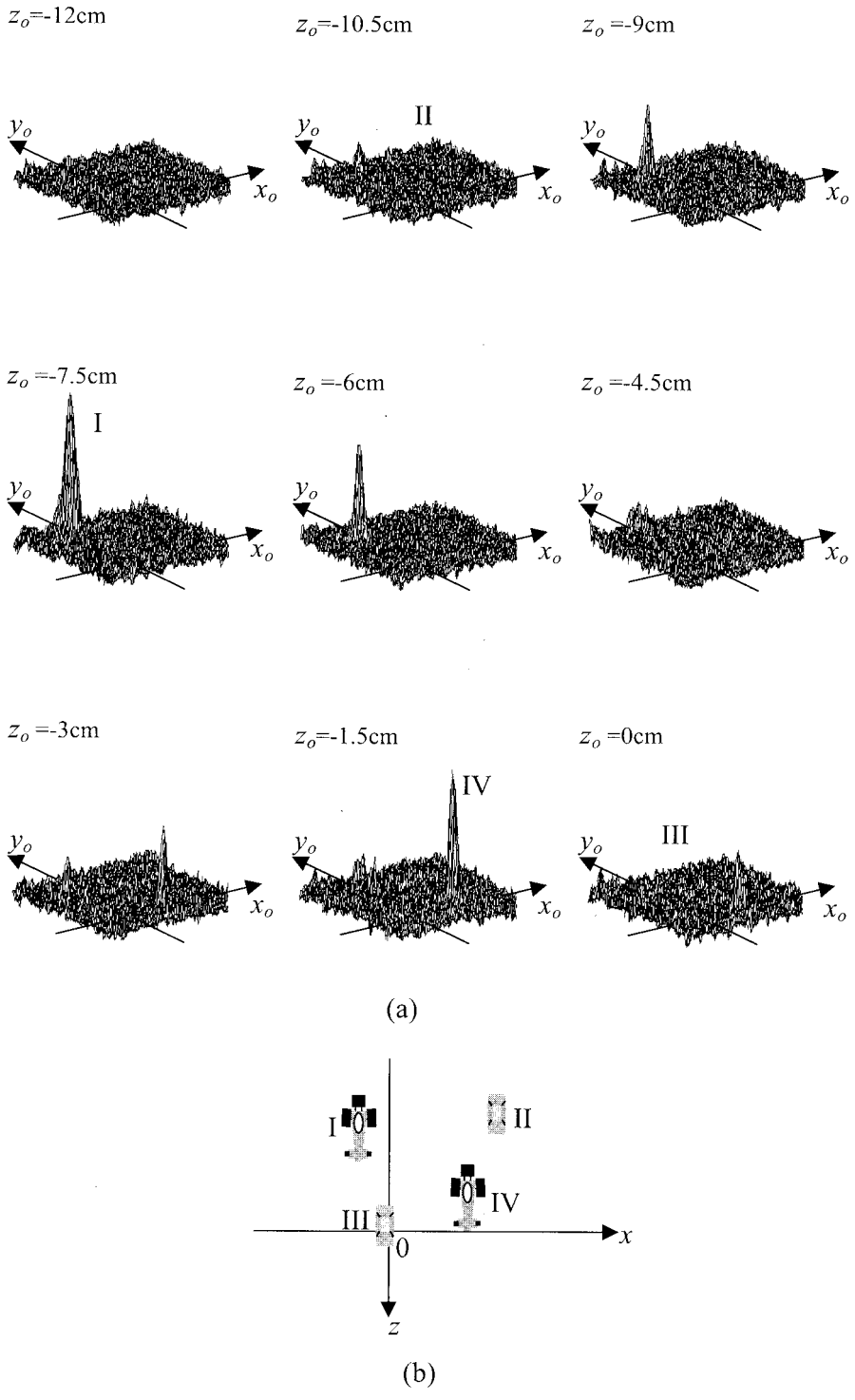

Fig. 7. (a) Intensity distributions about the first diffraction orders of nine correlation planes for several values of longitudinal axis z_0 as a result of the first experiment with the 3-D correlator. (b) Top view of the observed scene in the first experiment.

digital subtraction of the constant term $|A|^2$ from the function $I_4(u, v, \theta)$.

Spatial filtering is the next stage in the correlation process, and the nature of the filter should be determined. Most filters used for pattern recognition in 2-D correlators are complex valued, with nonzero imaginary parts. This is true for hundreds of filters proposed in recent years[12] designed to satisfy many criteria and computed by numerous computational methods. In many cases the complex filters are coded on real positive computer-generated holograms only to avoid the problem of using a complex-valued optical transparency. However, in our case the spatial spectrum is already recorded inside the com-

puter, and therefore there is no such constraint on the optical transparency at this stage of the system. We choose for the present demonstration a 3-D extension of the 2-D phase-only filter (POF).[13] This choice of filter is made only to illustrate an example of a general complex filter, and the same correlator can be equipped with different filters according to other needs. In fact, the reference function, obtained by the inverse FT of the POF, is just a real, bipolar function. However, the process presented here is valid for general complex reference functions, as well.

The 3-D phase-only filter of an object function $f(x, y, z)$ is defined as

$$H(u, v; \theta) = F^*(u, v; \theta)/|F(u, v; \theta)|, \tag{8}$$

where

$$F(u, v; \theta) = \int_{-\infty}^{\infty}\int_{-\infty}^{\infty}\int_{-\infty}^{\infty} f(x, y, z)\exp\left[i\,\frac{2\pi M}{\lambda f}\,(ux\cos\theta + vy + uz\sin\theta)\right]\mathrm{d}x\mathrm{d}y\mathrm{d}z. \tag{9}$$

Multiplying the hologram distributions (less the bias term) by the complex POF function yields

$$T_4(u, v, \theta) = H(u, v, \theta)[I_4(u, v, \theta) - |A|^2]. \tag{10}$$

The product $T_4(u, v, \theta)$ is intended to be Fourier transformed once again to yield the correlation function. At this point we notice that a coordinate transformation should be made before the final Fourier transform is performed. That is so because both functions $G_1(u, v, \theta)$ and $F(u, v, \theta)$ have the form of a 3-D FT with Fourier coordinates ($u \cos\theta$, v, $u \sin\theta$), but the real coordinates of the physical space at plane P_4 are (u, v, θ). Therefore, to get the desired 3-D FT, we must transform the function $T_4(u, v, \theta)$ from coordinate system (u, v, θ) to ($u \cos\theta$, v, $u \sin\theta$). Following the coordinate transformation, $T_4(u, v, \theta)$, denoted now $\tilde{T}_4(u\cos\theta, v, u\sin\theta)$, becomes

$$\begin{aligned}\tilde{T}_4(u\cos\theta, v, u\sin\theta) &= |\tilde{G}_1(u\cos\theta, v, u\sin\theta)|^2\tilde{H}(u\cos\theta, v, u\sin\theta)\\ &+ A^*\tilde{G}_1(u\cos\theta, v, u\sin\theta)\tilde{H}(u\cos\theta, v, u\sin\theta)\exp\left(-i\,\frac{2\pi}{\lambda}\,v\sin\psi\right)\\ &+ A\tilde{G}_1{}^*(u\cos\theta, v, u\sin\theta)\tilde{H}(u\,cos\,\theta, v, u\sin\theta)\exp\left(i\,\frac{2\pi}{\lambda}\,v\sin\psi\right),\end{aligned} \tag{11}$$

where $\tilde{G}_1$ and $\tilde{H}$ denote the functions of the image's spectrum and the filter at the new coordinate system, respectively.

We keep in mind that $\tilde{T}_4$ is going to be displayed on SLM2, which is again a transparency medium that can get only positive real values. Consequently, only the real part of $\tilde{T}_4$ can be displayed on SLM2. Thus from the three terms of $\tilde{T}_4$, $\mathrm{Re}\{\tilde{T}_4\}$ becomes an expression of six terms, the three of $\tilde{T}_4$ plus their complex-conjugate terms. Without additional processing in $\tilde{T}_4$ as given by Eq. (11), the important term of the convolution between $g_1(x, y, z)$ and $h(x, y, z)$ will be obscured by the convolution between $g_1(-x, -y, -z)$ and $h(x, y, z)$. To avoid this overlap between the correlation terms, we multiply $\tilde{T}_4$ by a linear phase function $\exp[i4\pi v\,(\sin\psi)/\lambda]$. Multiplying $\tilde{T}_4$ by this linear phase function causes a shift of all the correlation terms to one half of the correlation plane, whereas taking the real part of $\tilde{T}_4$ produces an additional set of correlation terms in the other half of the correlation plane. Thus the distribution in this stage becomes

$$\begin{aligned}\tilde{T}_4{}'(u\cos\theta, v, u\sin\theta) &= 2\,\mathrm{Re}\{\tilde{T}_4(u\cos\theta, v, u\sin\theta)\exp[i4\pi v(\sin\psi)/\lambda]\}\\ &= |\tilde{G}_1(u\cos\theta, v, u\sin\theta)|^2\tilde{H}(u\cos\theta, v, u\sin\theta)\exp[i4\pi v(\sin\psi)/\lambda]\\ &+ |\tilde{G}_1(u\cos\theta, v, u\sin\theta)|^2\tilde{H}^*(u\cos\theta, v, u\sin\theta)\exp[-i4\pi v(\sin\psi)/\lambda]\\ &+ A^*\tilde{G}_1(u\cos\theta, v, u\sin\theta)\tilde{H}(u\cos\theta, v, u\sin\theta)\exp[i2\pi v(\sin\psi)/\lambda]\\ &+ A\tilde{G}_1{}^*(u\cos\theta, v, u\sin\theta)\tilde{H}^*(u\cos\theta, v, u\sin\theta)\exp[-i2\pi v(\sin\psi)/\lambda]\\ &+ A\tilde{G}_1{}^*(u\cos\theta, v, u\sin\theta)\tilde{H}(u\cos\theta, v, u\sin\theta)\exp[i6\pi v(\sin\psi)/\lambda]\\ &+ A^*\tilde{G}_1(u\cos\theta, v, u\sin\theta)\tilde{H}^*(u\cos\theta, v, u\sin\theta)\exp[-i6\pi v(\sin\psi)/\lambda].\end{aligned} \tag{12}$$

Another 3-D inverse FT of $\tilde{T}_4{}'$ yields six diffraction orders that are spatially separated from one another along the y_0 axis, because of the different linear phase factors that multiply each term. In our setup, this final 3-D FT is performed in two steps. First, a one-dimensional digital FT from $u \sin\theta$ to z_0 is performed

as follows:

$$\tilde{T}_5(u\cos\theta, v, z_0) = \int_{-\infty}^{\infty} \tilde{T}_4'(u\cos\theta, v, u\sin\theta) \times \exp\left[-i\frac{2\pi M}{\lambda f}(z_0 u\sin\theta)\right] \times \mathrm{d}(u\sin\theta). \quad (13)$$

The remaining 2-D FT's from $(u\cos\theta, v)$ to (x_0, y_0) are done optically, where each 2-D FT is made for a different value of z_0. For any value of z_0, the 2-D function $\tilde{T}_5(u\cos\theta, v, z_0)$, plus a proper bias C, to ensure positive values, is displayed on SLM2. Then, with lens L_2, a series of 2-D FT's is obtained in the output. The number of 2-D transforms in the sequence is actually related to the measure of z_0. When one has only a single SLM, the series of 2-D optical FT's is considered sequentially, one at a time; otherwise the FT's can be treated in parallel.

For our purposes, the interesting term in Eq. (12) is the third one, inasmuch as that term yields the desired convolution between $g_1(x, y, z)$ and $h(x, y, z)$. Because of the spatial separations among all the output terms, we let ourselves ignore all the terms other than the third one. Some of the higher-order terms may even be eliminated because of the low sampling rate of SLM2. Therefore correlation results are obtained from an inverse 3-D FT of the third term as follows:

$$\begin{aligned} c(x_0, y_0, z_0) \propto \int_{-\infty}^{\infty}\int_{-\infty}^{\infty} \Bigg\{ \int_{-\infty}^{\infty} \tilde{G}_1(u\cos\theta, v, u\sin\theta) \\ \times \tilde{H}(u\cos\theta, v, u\sin\theta)\exp[i2\pi v(\sin\psi)/\lambda] \\ \times \exp\left[-i\frac{2\pi M}{\lambda f}(z_0 u\sin\theta)\right]\mathrm{d}(u\sin\theta)\Bigg\} \\ \times \exp\left[-i\frac{2\pi M}{\lambda f}(x_0 u\cos\theta + y_0 v)\right]\mathrm{d}(u\cos\theta)\mathrm{d}v \\ = \Bigg[\int_{-\infty}^{\infty}\int_{-\infty}^{\infty}\int_{-\infty}^{\infty} g_1(x, y, z)h(x_0 - x, y_0 - y, z_0 \\ - z)\mathrm{d}x\mathrm{d}y\mathrm{d}z\Bigg] * \delta[x_0, y_0 - f(\sin\psi)/M, z_0]. \end{aligned} \quad (14)$$

The desired correlation result is obtained about the point

$$(x_0, y_0, z_0) = [0, f(\sin\psi)/M, 0].$$

3. Experimental Results

Three experiments in different experimental conditions were carried out with the system shown in Fig. 1. We first describe the first experiment in detail and then present the input images and the final results of the other two experiments.

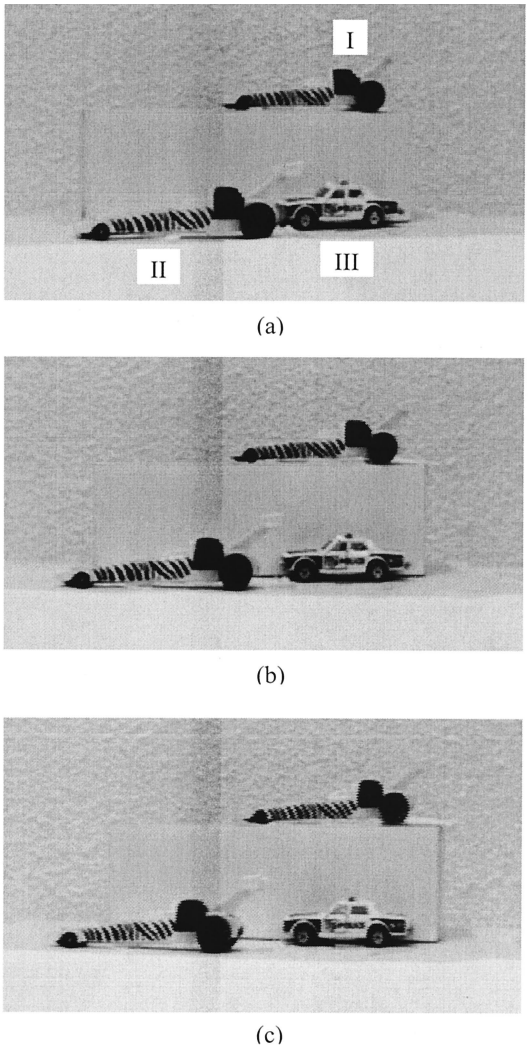

(a)

(b)

(c)

Fig. 8. Three images of twenty-one of the input scene in the second experiment, as observed from different points of view from plane P_2 at angles (a) $\theta = -10°$, (b) $\theta = 0°$, and (c) $\theta = 10°$.

In the first experiment the observed scene contained four toy cars, I–IV, in various locations. The two race cars, I and IV, were used here as the objects to be recognized, whereas the two patrol cars, II and III, were the false objects. Cars I, II, III, and IV were located at distances 57.5, 60.5, 50, and 51.5 cm, respectively, from the camera. The distance between the point of origin of the scene and the CCD on plane P_2 was 50 cm. Three examples of thirty-one projections from the first experiment are shown in Fig. 2. Figures 2(a), 2(b), and 2(c) show the scene as viewed by the CCD positioned at θ angles of $-15°$, $0°$, and $15°$, respectively, from the optical axis. The angular increment between successive projections was $1°$, and the angles of $\pm 15°$ were the extreme angles of this experiment.

All the 31 projections were sequentially displayed on SLM1. From SLM1, each projection was optically Fourier transformed by lens L_1 and interfered with the reference plane wave on CCD plane P_4. As a result, 31 electronic Fourier holograms of the

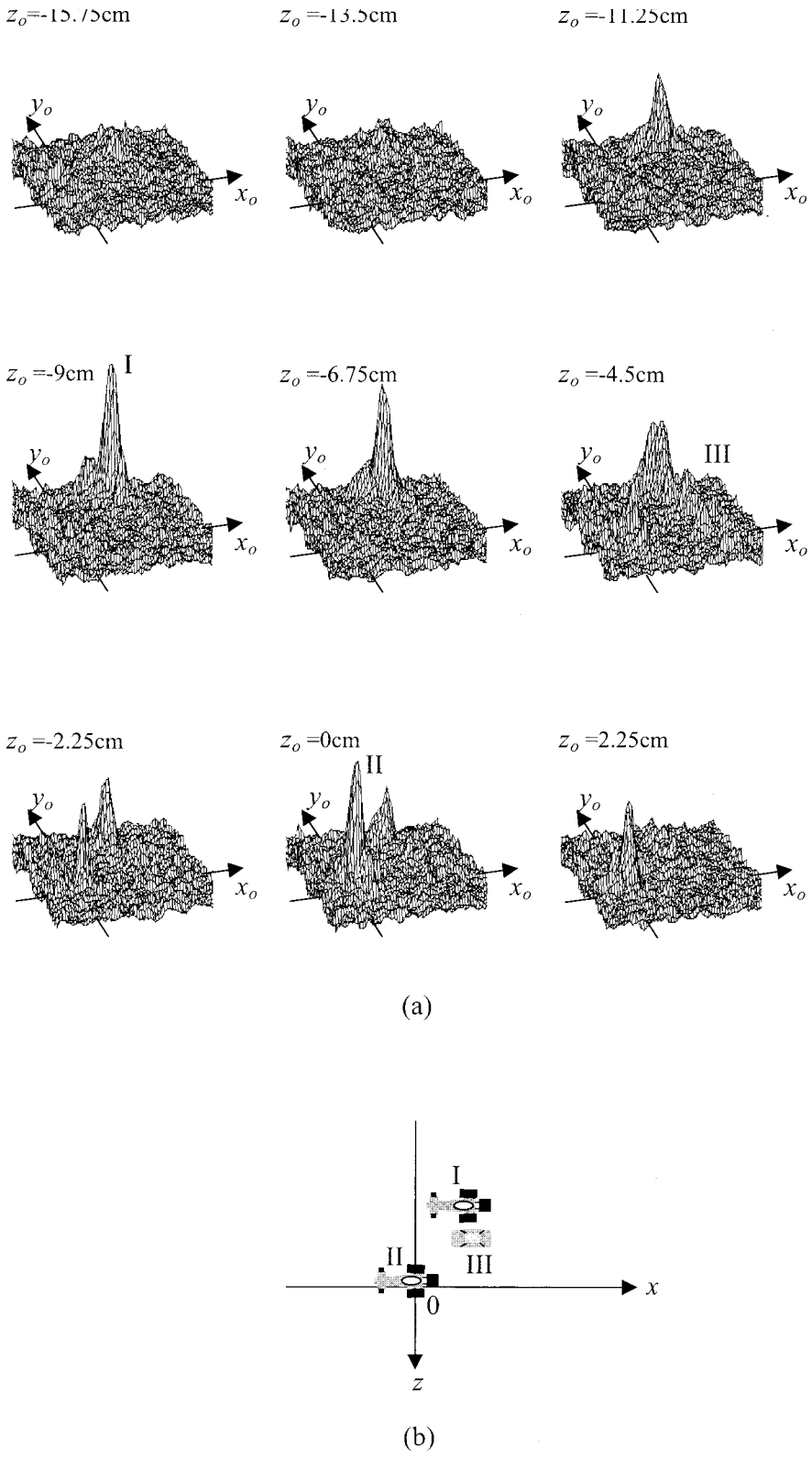

Fig. 9. (a) Intensity distribution of nine correlation planes, for different values of z_0, that resulted from the second experiment with the 3-D correlator. (b) Top view of the observed scene in the second experiment.

various projections were recorded in the computer. Three of the holograms, corresponding to the three projections of Fig. 2, are shown in Fig. 3. From each hologram, first the bias was subtracted and then the functions were multiplied by POF's. Every filter was computed for each projection of the same race car positioned at $(x, y, z) = (0, 0, 0)$, according to Eq. (8). The phase distribution of the

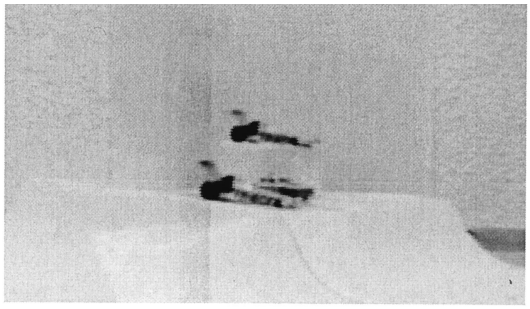

(a)

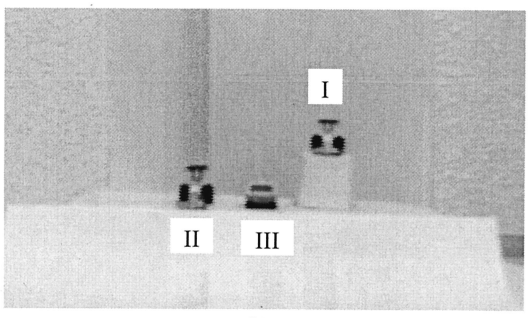

(b)

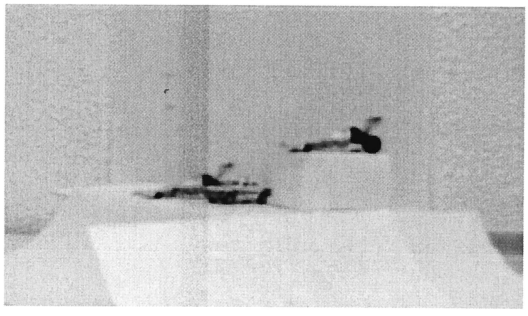

(c)

Fig. 10. Three images of twenty-one of the input scene in the third experiment, as observed from different points of view from plane P_2 at angles (a) $\theta = -50°$, (b) $\theta = 0°$, and (c) $\theta = 50°$.

computed 256 × 256 pixel POF's of the extreme left-hand, central, and extreme right-hand projections are shown in Figs. 4(a), (4b), and (4c), respectively. After multiplying all the 31 holograms by the proper complex POF's, we performed the coordinate transformation mentioned in Section 2. As a result of the coordinate transformation, all the current data were organized into a 3-D complex-valued matrix of the size 256 × 256 × 67 pixels. The value 67 is the size of the longitudinal frequency axis approximated by the number $\max(u) \times \sin[\max(\theta)] = 256 \times \sin(15°)$ according to the coordinate transformation. This value is actually the longitudinal bandwidth of the system, and it indicates the resolving power of the system along the longitudinal axis. More precisely, if the size of a pixel on plane P_4 is d, then, according to Eq. (6), the smallest size along the z axis that the system can resolve is $\lambda f/67dM$. The distance between two pixels determines the maximum size of the input object that the system can process. If d is also the distance between the pixels along the longitudinal frequency axis, then the maximum object's depth that can be handled is $\lambda f/dM$.

To get good separation among the various convolution terms on the output plane, we multiplied the current function by the linear phase function $\exp[i4\pi v(\sin \psi)/\lambda]$. Then to obtain the final correlation results we needed to perform a 3-D FT on the last matrix. As mentioned in Section 2, we first performed a digital one-dimensional FT from $(u \cos \theta, v, u \sin \theta)$ to $(u \cos \theta, v, z_0)$. At this point, the real parts of the obtained 2-D functions, plus some bias (to ensure a positive-valued matrix), were displayed successively on SLM2, each pattern for a different value of z_0. Nine patterns of the given sixty-seven z_0 values are shown in Fig. 5.

The correlation results are depicted in Fig. 6 and 7. Figure 6 shows the intensity distribution on output plane P_6, corresponding to the transverse planes with the same z_0 values as in Fig. 5. Only the three central diffraction orders are shown here. From Eq. (12) it is clear that each diffraction pattern at any z_0 value should be symmetric about the origin. Therefore we can use the area of the two first diffraction orders as the region in which to look for the recognition peaks. The strongest peaks in the two first diffraction orders are found at $z_0 = -1.5$ and $z_0 = -7.5$ cm. These are the summits of the two recognition peaks of race cars IV and I, respectively. The area of the lower first diffraction order was used as the data for the series of 3-D plots shown in Fig. 7(a). Each 3-D plot shows the intensity distribution on a transverse plane along the z_0 axis. Two recognizable peaks appear in the locations of the two true class objects I (at $z_0 = -7.5$ cm) and IV (at $z_0 = -1.5$ cm), whereas false cars II and III did not grow peaks above the noise level. Every correlation peak has a finite width in all its three dimensions. In addition to the ordinary dependence of this width on the size of the correlated functions, the width along z_0 is inversely dependent on the angular range of the observing cameras, which was 30° in the first experiment. The other clearly shown peaks in Fig. 7, at $z_0 = -6$ cm and $z_0 = -9$ cm, are part of the same identification peak whose summit appears at $z_0 = -7.5$ cm. Similarly, the peaks at $z_0 = 0$ and $z_0 = -3$ cm are part of the same identification peak whose summit appears at $z_0 = -1.5$ cm. To facilitate observation of the 3-D correlation plots, a schematic of the input scene from a top view is included in Fig. 7(b).

In the second experiment the observed scene was viewed from a different direction from that of the first test. This time the depth dimension of each car was smaller than the width. Therefore, within an angular interval of 20°, the cars seem almost the same along the various points of view. The distance between the origin point of the scene and the CCD was only 46.5 cm this time. Three examples out of the twenty-one projections from the second experiment are shown in Fig. 8. Figures 8(a), 8(b), and 8(c) show the scene seen by the CCD positioned at θ angles of

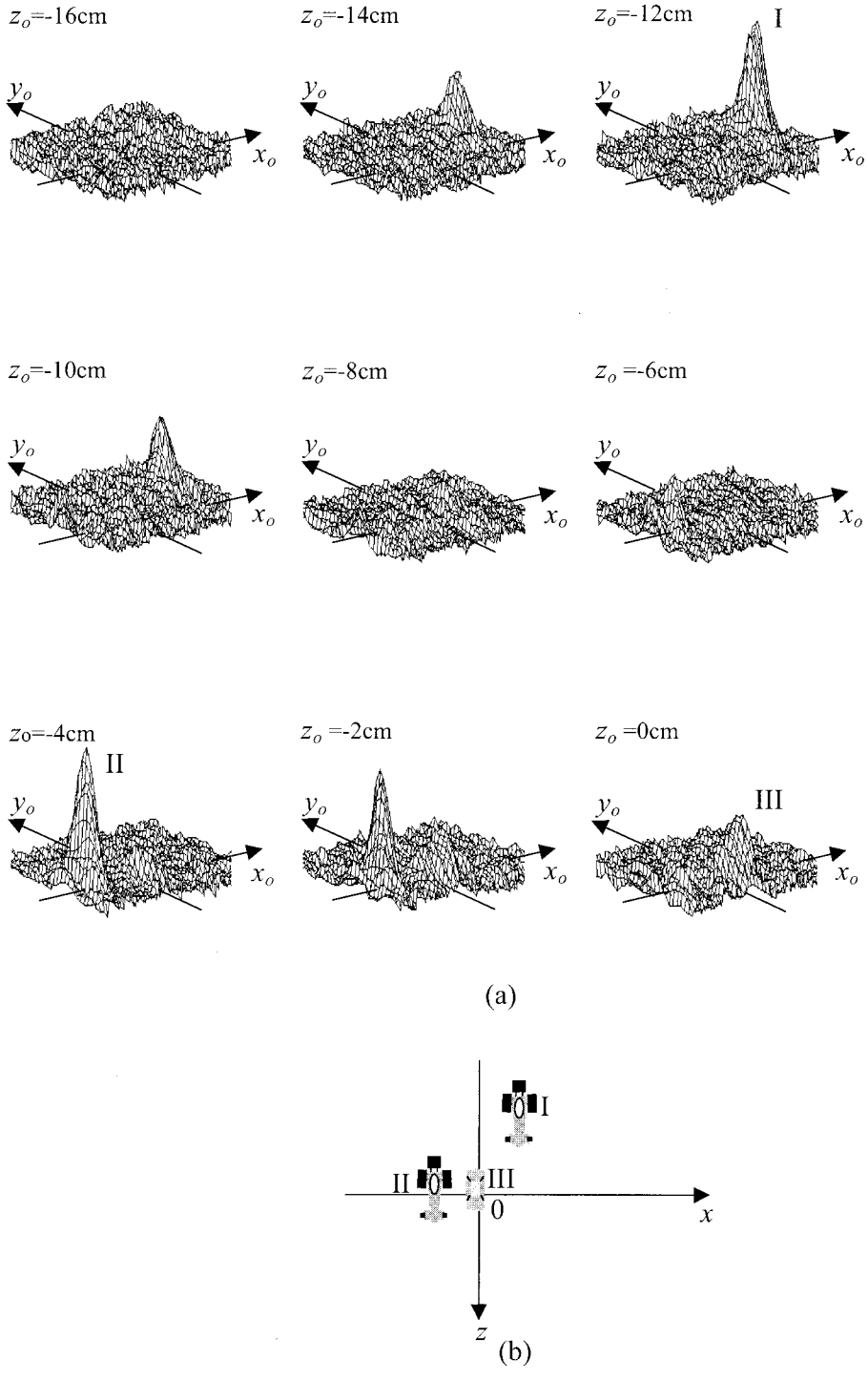

Fig. 11. (a) Intensity distribution of nine correlation planes, for several values of z_0 that resulted from the third experiment with the 3-D correlator. (b) Top view of the observed scene in the third experiment.

$-10°$, $0°$, and $10°$, respectively, from the optical axis. As in the first experiment, we succeeded in identifying the two true objects and their locations, as shown in Fig. 9. Nine 3-D plots of correlation transverse planes along different z_0 values are shown in Fig. 9(a). Two recognizable peaks appear in the locations of the two true class objects, I and II, at $z_0 = -9$ cm and $z_0 = 0$. False car III has a false peak at $z_0 = -4.5$ cm, which is 2.36 times weaker than the minimal between the two true peaks.

In the final experiment we considered the nonparaxial case for which the angular range $\pm\theta$ is significantly larger than the small-angle range demonstrated in the first two experiments. Under these conditions the small-angle approximation is not valid. Therefore the coordinate transforma-

tion must be performed from (u, v, θ) to $(u \cos \theta, v, u \sin \theta)$. Because of limitations in our digital memory size we were forced to reduce the number of simultaneous projections with increasing angular range. Also, we reduced the sizes of the images by recording the images from a longer distance. This time the distance between the origin point of the scene and the CCD was 107 cm. In this experiment 21 projections were recorded in 5° increment between successive projections and in a total angular range of ±50°. Three examples of these projections are shown in Fig. 10. Figures 10(a), 10(b), and 10(c) show the scene seen by the CCD positioned at θ angles of −50°, 0°, and 50°, respectively, from the optical axis. Note that it may happen as in this example that parts of the objects will be hidden by other cars in several projections. However, the correlation process is based on all the projections, and therefore the recognition is accomplished as demonstrated in Fig. 11. The maximum values of true object peaks appear at $z_0 = -4$ cm for object II and at -12 cm for object I, whereas the false object peak is seen at $z_0 = 0$. The discrimination ratio between the true and the false peaks is 1.67.

4. Conclusions

In conclusion, we have demonstrated a process of 3-D electro-optical correlation between a real-world 3-D function and a general 3-D complex reference function. It should be noted that, unlike in previous experiments,[1–3,6] here, for what we believe is the first time, we present a complete electro-optical correlation process with all the necessary optical 2-D FT's. To achieve this goal with the available SLM technology, we propose a new electro-optical correlator design. This design is a combination of a JTC and a VLC. From an optics viewpoint, the use of electronic holograms has been introduced into the first part of a 3-D correlator, and the digital processing has been aimed to code computer-generated holograms for its second optical part. From the electronics viewpoint, it seems at first glance that many digital operations have been added to this new design. However, most of the computational task of the 3-D scene is still done optically by the two parallel 2-D FT processors, and part of the digital operations is aimed to permit use of real positive optical transparencies.

The new correlator was tested in three independent experiments under different conditions. The third experiment has shown that the proposed correlator can operate under nonparaxial conditions as well.

This research was supported by the Israel Science Foundation. The reviewers' comments are highly appreciated.

References

1. J. Rosen, "Three-dimensional optical Fourier transform and correlation," Opt. Lett. **22,** 964–966 (1997).
2. J. Rosen, "Three-dimensional electro-optical correlation," J. Opt. Soc. Am. A **15,** 430–436 (1998).
3. J. Rosen, "Three-dimensional joint transform correlator," Appl. Opt. **37,** 7538–7544 (1998).
4. T. C. Poon and T. Kim, "Optical image recognition of three-dimensional objects," Appl. Opt. **38,** 370–381 (1999).
5. J. J. Esteve-Taboada, D. Mas, and J. Garcia, "Three-dimensional object recognition by Fourier transform profilometry," Appl. Opt. **38,** 4760–4765 (1999).
6. Y. Li and J. Rosen, "Three-dimensional pattern recognition with a single two-dimensional synthetic reference function," Appl. Opt. **39,** 1251–1259 (2000).
7. D. Mendlovic, E. Marom, and N. Konforti, "Complex reference-invariant joint-transform correlator," Opt. Lett. **15,** 1224–1226 (1990).
8. U. Mahlab, J. Rosen, and J. Shamir, "Iterative generation of complex reference functions in a joint-transform correlator," Opt. Lett. **16,** 330–332 (1991).
9. A. B. VanderLugt, "Signal detection by complex spatial filtering," IEEE Trans. Inf. Theory **IT-10,** 139–145 (1964).
10. J. W. Goodman, *Introduction to Fourier Optics*, 2nd ed. (McGraw-Hill, New York, 1996), Chap. 8, p. 237.
11. J. Rosen, T. Kotzer, and J. Shamir, "Optical implementation of phase extraction pattern recognition," Opt. Commun. **83,** 10–14 (1991).
12. B. V. K. Vijaya Kumar, "Tutorial survey of composite filter designs for optical correlators," Appl. Opt. **31,** 4773–4801 (1992).
13. J. L. Horner and P. D. Gianino, "Phase-only matched filtering," Appl. Opt. **23,** 812–816 (1984).